Tenth International Conference on Computational Fluid Dynamics (ICCFD10), Barcelona, Spain, July 9-13, 2018

ICCFD10-155

Domain-Decoupled Compact Schemes for Parallel Simulation of Turbulence

J. Fang*, F. Gao**, C. Moulinec* and D. R. Emerson*
Corresponding author: jian.fang@stfc.ac.uk

*Scientific Computing Department, STFC Daresbury Laboratory, Warrington WA4 4AD, United Kingdom
**Faculty of Engineering and Physical Sciences, University of Surrey, Guildford GU2 7XH, United Kingdom

Abstract: A class of domain-decoupled compact schemes for first and second spatial derivatives is proposed for a domain-decomposition-based parallel computational fluid dynamics solver, improving the accuracy of a previously developed decoupled compact scheme. The proposed schemes preserve the accuracy and bandwidth properties of fully coupled compact schemes, even for very large degrees of parallelism, and enables the Navier-Stokes equations to be solved independently on each processor. The schemes are analysed by using Fourier analysis, tested on 2-D convection/diffusion problems, and assessed in the direct numerical simulation (DNS) of the Taylor-Green vortex problem. The results prove its effectiveness in the DNS of turbulence in terms of accuracy and good scalability.

Keywords: Compact scheme; Domain-decoupled; Parallel computation; Direct numerical simulation

1 Introduction

Compact or Padé-type schemes [1] with spectral-like resolution are highly desirable in computational fluid dynamics (CFD), especially direct numerical [2,3]/large-eddy simulation [4,5] (DNS/LES) of turbulence and computational aeroacoustics (CAA) [6], in which small-scale flow structures need to be resolved. However, compact schemes are spatially coupled, which means the numerical derivatives are acquired via solving either a tridiagonal or pentadiagonal linear system. In serial environment, the Thomas algorithm can be efficiently used to solve a tridiagonal linear system, but difficulties arise in a domain-decomposition-based MPI parallel environment. In both forward sweep and back substitution of the Thomas algorithm, the solution of a local node depends on solutions from its neighbouring nodes. Therefore, for a domain-decomposition-based parallel solver, only one processor can do the differentiation operation at one time and all the others have to wait.

Significant effort has been devoted to the parallelisation of compact schemes. These methods can be categorised into two groups. The first group focuses on the way of solving a tridiagonal matrix, using wither the block pipeline method [7], the parallel diagonal dominant algorithm [8], or the line-relaxation method [9]. The second group decouples the compact scheme to enable the scheme to be solved independently on each processor. The latter approach has shown superior parallel performance as demonstrated by Sengupta *et al.* [10], Chao *et al.* [11] and Kim and Sandberg [12]. Sengupta *et al.* [10] used a large overlap of subdomains and a biased boundary

scheme to decouple the compact scheme but this resulted higher errors on a finer mesh. Chao *et al.* [11] used an explicit scheme at the block interface to decouple the corresponding compact scheme. For the convective fluxes, they used an explicit fifth-order upwind scheme at the interface nodes to decouple the fifth-order compact upwind scheme, hybridising with a WENO scheme to capture shock-waves. For the computation of diffusive fluxes, a sixth-order explicit central scheme at the block interface was used to decouple the sixth-order compact central scheme. Their decoupling method has shown good stability and scalability [11]. Kim and Sandberg [12] recently proposed a fourth-order parallel compact scheme, which uses a fourth-order spline function to extrapolate the derivatives in the halo area to decouple the scheme. Their scheme produced smooth flow field across the interface and its good performance in DNS [13], LES [14] and CAA [15,16] simulations was demonstrated.

Although good parallel performance has been observed by the decoupled compact schemes mentioned above, a degradation in spectral performance has been found, for example in Chao *et al.*'s scheme as shown in Figures 3-6, on the interface nodes between computational blocks. Inspired by Chao *et al.* [11] and Kim and Sandberg [12], the present paper presents a modified class of domain-decoupled compact schemes for domain-decomposition-based CFD solver, which uses an explicit scheme with the same order of accuracy in halo nodes to close the tridiagonal system in each subdomain, aiming at improving the accuracy of the decoupled compact scheme on the interface node of blocks. Our analysis and tests demonstrate that the proposed scheme has bandwidth properties and truncation errors close to the fully coupled scheme. The scalability is ensured owing to the fact that the scheme is decoupled at the interface of each subdomain. The scheme is assessed on a 2-D vortex convection/diffusion problem, and the 3-D Taylor-Green Vortex problem, showing its effectiveness in solving compressible Navier-Stokes equations as well as its good scalability.

2 Domain-Decoupled Compact Scheme

In this section, the principle of the proposed decoupled compact (DCOM) schemes for both first and second derivatives is going to be introduced in general forms and the details of sixth-order DCOM central schemes are also given.

2.1 First derivative

For a general continuous differentiable function ϕ discretised on a uniform 1-D mesh $x_i = i\Delta, i = 0,1,\cdots,N$, in which Δ is the distance between two consecutive mesh nodes, the derivative ϕ' at the i-th mesh node (internal node) is approximated using the following general compact central scheme,

$$\alpha\tilde{\phi}'_{i-1} + \tilde{\phi}'_i + \alpha\tilde{\phi}'_{i+1} = \frac{a}{\Delta}(\phi_{i+2} - \phi_{i-2}) + \frac{b}{\Delta}(\phi_{i+1} - \phi_{i-1}), \quad (1)$$

where $\tilde{\phi}'_i$ is the approximation of ϕ' at x_i, and α, a and b are coefficients defining a specific scheme. Although compact schemes have the advantages of smaller stencils, higher bandwidth resolution, and smaller truncation error over the explicit scheme of the same order, their drawback is the implicit solution of Eq. (1). The following linear algebra system needs to be solved to obtain $\tilde{\phi}'_i$.

$$\mathbf{AX} = \mathbf{Y}, \quad (2)$$

in which $\mathbf{A} = \begin{bmatrix} 1 & \alpha_0 & 0 & & & 0 \\ \alpha_1 & 1 & \alpha_1 & & & \\ 0 & \alpha & 1 & \alpha & & \\ & & \ddots & & & \\ & & \alpha & 1 & \alpha & 0 \\ & & & \alpha_1 & 1 & \alpha_1 \\ 0 & & & 0 & \alpha_0 & 1 \end{bmatrix}$ is a tridiagonal matrix, $\mathbf{X} = \begin{bmatrix} \tilde{\phi}'_0 \\ \tilde{\phi}'_1 \\ \tilde{\phi}'_2 \\ \vdots \\ \tilde{\phi}'_{N-2} \\ \tilde{\phi}'_{N-1} \\ \tilde{\phi}'_N \end{bmatrix}$ is the solution vector to be solved, and **Y** is the known term on the right-hand-side of Eq. (2). α_0 and α_1 in **A** are used for nodes close to the physical boundaries. Equation (2) can be solved efficiently using the classic Thomas algorithm in a serial environment, but difficulties arise in parallel, limiting processors to work sequentially.

The principle of the new scheme is presented. For the domain-decomposition-based parallel environment, assuming that a 1-D domain discretized with N nodes is decomposed into M subdomains. Figure 1 shows the distribution of the nodes around the interface between subdomains k and $k+1$, with $\phi_i, i = -4, -3, \cdots, N_k + 4$ defined on subdomain k. Four halo nodes at each side of the subdomain are used to exchange data from neighboring subdomains, targeting a sixth-order central scheme. More halos nodes could also be defined for higher order schemes.

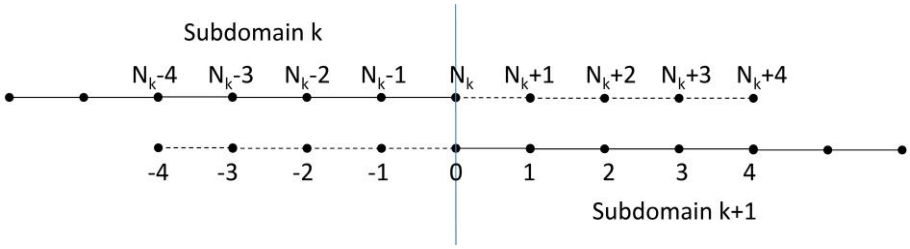

Figure 1: Schematic representation of the overlap region between two subdomains.

To decouple the compact scheme in subdomain k, an explicit central scheme (ECS) with the same order as the compact scheme is implemented for $i = -1$ and $N_k + 1$ halo nodes to close the tridiagonal matrix in subdomain k. The procedure of implementing the DCOM scheme is given as follows and shown in Figure 2,

a) At the first layer of halo nodes $i = -1$ and $N_k + 1$, the ECS of the same order as the compact scheme is used to compute $\tilde{\phi}'_{-1}$ and $\tilde{\phi}'_{N_k+1}$ as,

$$\tilde{\phi}'_{-1} = \frac{1}{\Delta}\sum_{m=1}^{3} c_m(\phi_{-1+m} - \phi_{-1-m}), \tag{3}$$

and

$$\tilde{\phi}'_{N_k+1} = \frac{1}{\Delta}\sum_{m=1}^{3} c_m(\phi_{N_k+1+m} - \phi_{N_k+1-m}), \tag{4}$$

respectively, where c_m is the coefficient defining an explicit central scheme.

b) At the interface nodes $i = 0$ and N_k, Eq. (1) can be reduced to,

$$\tilde{\phi}'_0 + \alpha\tilde{\phi}'_1 = \frac{a}{\Delta}(\phi_2 - \phi_{-2}) + \frac{b}{\Delta}(\phi_1 - \phi_{-1}) - \alpha\tilde{\phi}'_{-1}, \tag{5}$$

and

$$\tilde{\phi}'_{N_k} + \alpha\tilde{\phi}'_{N_k-1} = \frac{a}{\Delta}(\phi_{N_k+2} - \phi_{N_k-2}) + \frac{b}{\Delta}(\phi_{N_k+1} - \phi_{N_k-1}) - \alpha\tilde{\phi}'_{N_k+1}. \tag{6}$$

c) The decoupled tridiagonal matrix is, therefore, able to be solved independently in each subdomain with the classic Thomas algorithm.

d) Correction Step:

d1. Update $\tilde{\phi}'_{-1}$ and $\tilde{\phi}'_{N_k+1}$ by swapping data with neighboring nodes, e.g. exchanging $\tilde{\phi}'_{-1}$ and $\tilde{\phi}'_{N_k+1}$ in the subdomain k with $\tilde{\phi}'_{N_{k-1}-1}$ in the

subdomain $k-1$ and $\tilde{\phi}'_1$ in the subdomain $k+1$, respectively.

d2. Repeat steps b) and c) to re-calculate the tridiagonal matrix and update $\tilde{\phi}'_i$.

e) The final interface value is acquired by averaging $\tilde{\phi}'_{N_k}$ from the subdomain k and $\tilde{\phi}'_0$ from the subdomain $k+1$.

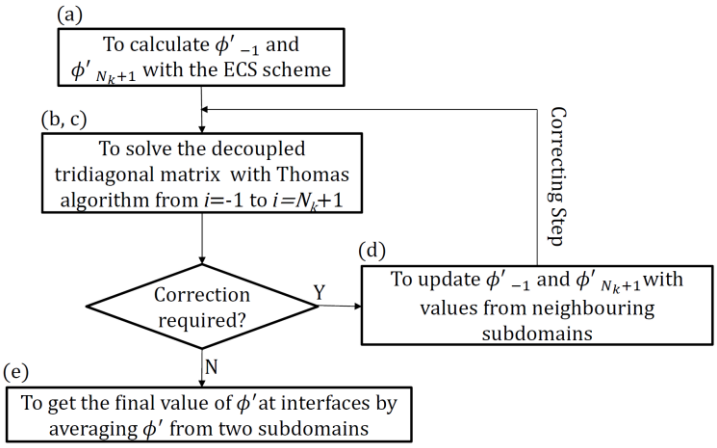

Figure 2: Procedure of implementing DCOM scheme.

In the above procedure, the correction steps (d1 and d2) can be avoided or run many times, depending on the accuracy required and computing time available.

The proposed scheme without the correction step is similar to the one proposed by Chao *et al.* [11], but differing in the position where the explicit scheme is implemented: $i=-1$ and $i=N_k+1$ for the present scheme; $i=0$ and $i=N_k$ for the scheme of Chao *et al.* [11]. A comparison of the two schemes will be given in the next part of the paper.

The implementation of a sixth-order DCOM scheme (DCOM6) is detailed as follows.

$\tilde{\phi}'_{-1}$ and $\tilde{\phi}'_{N_k+1}$ are calculated with the sixth-order explicit central scheme (ECS6):

$$\tilde{\phi}'_{-1}=\frac{\phi_2-\phi_{-4}}{60\Delta}-3\frac{\phi_1-\phi_{-3}}{20\Delta}+3\frac{\phi_0-\phi_{-2}}{4\Delta}, \tag{7}$$

and

$$\tilde{\phi}'_{N_k+1}=\frac{\phi_{N_k+4}-\phi_{N_k-2}}{60\Delta}-3\frac{\phi_{N_k+3}-\phi_{N_k-1}}{20\Delta}+3\frac{\phi_{N_k+2}-\phi_{N_k}}{4\Delta}. \tag{8}$$

At $i=0$ and $i=N_k$, the scheme reduces to,

$$\tilde{\phi}'_0+\frac{1}{3}\tilde{\phi}'_1=\frac{1}{36\Delta}(\phi_2-\phi_{-2})+\frac{7}{9\Delta}(\phi_1-\phi_{-1})-\frac{1}{3}\tilde{\phi}'_{-1}, \tag{9}$$

and

$$\frac{1}{3}\tilde{\phi}'_{N_k-1}+\tilde{\phi}'_{N_k}=\frac{1}{36\Delta}\left(\phi_{N_k+2}-\phi_{N_k-2}\right)+\frac{7}{9\Delta}\left(\phi_{N_k+1}-\phi_{N_k-1}\right)-\frac{1}{3}\tilde{\phi}'_{N_k+1}. \tag{10}$$

For internal nodes ($i=1,2,\cdots N_{k-1}$) in subdomain k, the classic sixth-order compact central scheme (COM6) [1] is implemented,

$$\frac{1}{3}\tilde{\phi}'_{i-1}+\tilde{\phi}'_i+\frac{1}{3}\tilde{\phi}'_{i+1}=\frac{1}{36\Delta}(\phi_{i+2}-\phi_{i-2})+\frac{7}{9\Delta}(\phi_{i+1}-\phi_{i-1}). \tag{11}$$

After solving Eqs. (7-9) using the Thomas algorithm, $\tilde{\phi}'_{-1}$ and $\tilde{\phi}'_{N_k+1}$ are updated with values in the neighboring subdomain and Eqs. (7-9) are re-calculated using the updated $\tilde{\phi}'_{-1}$ and $\tilde{\phi}'_{N_k+1}$ in the correction step. The final interface value is acquired by averaging $\tilde{\phi}'_{N_k}$ from subdomain k and $\tilde{\phi}'_0$ from the subdomain $k+1$.

2.2 Second derivative

For the approximation of the second derivative $\tilde{\phi}''$, the sixth-order compact and explicit schemes are respectively given as,

$$\frac{2}{11}\tilde{\phi}''_{i-1} + \tilde{\phi}''_{i} + \frac{2}{11}\tilde{\phi}''_{i+1} = 3\frac{\phi_{i+2} - 2\phi_i + \phi_{i-2}}{44\Delta^2} + 12\frac{\phi_{i+1} - 2\phi_i + \phi_{i-1}}{11\Delta^2}, \tag{12}$$

and

$$\tilde{\phi}''_{i} = \frac{\phi_{i+3} - 2\phi_i + \phi_{i-3}}{90\Delta^2} - 3\frac{\phi_{i+2} - 2\phi_i + \phi_{i-2}}{20\Delta^2} + 3\frac{\phi_{i+1} - 2\phi_i + \phi_{i-1}}{2\Delta^2}. \tag{13}$$

The same idea is applied to decouple Eq. (12) at the interface $i = 0$ as,

$$\tilde{\phi}''_{0} + \frac{2}{11}\tilde{\phi}''_{1} = 3\frac{\phi_{i+2} - 2\phi_i + \phi_{i-2}}{44\Delta^2} + 12\frac{\phi_{i+1} - 2\phi_i + \phi_{i-1}}{11\Delta^2} - \frac{2}{11}\tilde{\phi}''_{-1}, \tag{14}$$

and $\tilde{\phi}''_{-1}$ is calculated with the explicit scheme in Eq. (11). A symmetric operation is implemented for $i = N_k$ and $i = N_k + 1$. At the last step, the final interface values are averaged between the two neighboring subdomains.

3 Fourier Analysis of Schemes

The spectral properties of the proposed schemes are first analysed using the Fourier analysis. For the pure harmonic function,

$$\phi(x) = e^{ikx}, \tag{15}$$

its first and second derivatives are respectively expressed as,

$$\phi'(x) = ike^{ikx} = ik\phi(x), \tag{16}$$

and

$$\phi''(x) = -k^2e^{ikx} = -k^2\phi(x). \tag{17}$$

The approximation of $\phi'(x)$ and $\phi''(x)$ by a finite difference scheme can also be expressed in the modified wavenumber as,

$$\tilde{\phi}' = i\hat{k}\phi, \tag{18}$$

and

$$\tilde{\phi}'' = -\hat{k}^2\phi. \tag{19}$$

The relation between $\hat{k}$ and k can therefore be reduced to,

$$\hat{k} = -i\frac{\tilde{\phi}'}{\phi}. \tag{20}$$

and

$$\hat{k} = \sqrt{-\frac{\tilde{\phi}''}{\phi}}, \tag{21}$$

for the first and second derivatives respectively.

For linear schemes, an analytical expression can be obtained. However, the implementation of the DCOM scheme is related to the number of nodes in the subdomain and a general analytical spectral expression is therefore hard to acquire. To analyse the spectral property, $\tilde{\phi}'$ and $\tilde{\phi}''$ in Eqs. (16) and (17), with k changing from 0 to π, are numerically calculated by specific schemes in a 1-D domain $x \in [0,2\pi]$ discretized with N uniform cells, corresponding to $N + 1$ nodes. These nodes are distributed in M subdomains. Then $\hat{k}$ is calculated by using Eqs. (18) and (19), respectively. The mean values of $\hat{k}$ are obtained by averaging $\hat{k}$ on all nodes.

The spectral properties for the first derivatives with $N = 64$ are shown in Figure 3 (a). It considers subdomain number M equaling to 4 and 16, corresponding to $N_k = 16$ and 4 ($N_k = N/M$). The compact schemes show higher resolution at large wavenumbers than the explicit scheme of the same order. The DICOM scheme in the figure refers to the decoupled compact scheme of Chao *et al.* [11] and it falls between those of ECS6 and COM6 and approaches that of COM6 as N_k is increased. The DCOM6 scheme proposed in the present paper shows a better spectral performance than the DICOM6 scheme. Its spectral property is closer to that of the COM6 scheme and is less sensitive to N_k. Test with $N_k = 4$ shows that the implementation of the correction step can be used to effectively improve the accuracy of the DCOM scheme.

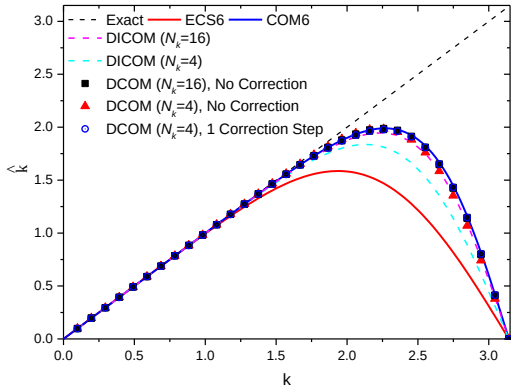

Figure 3: Mean values of $\hat{k}$ (real part) of sixth-order central schemes for first derivative.

The spectral property of the sixth-order schemes for the second derivative, $|\hat{k} - k|$, is presented in Figure 4. Similar results to the first derivative are observed. The mean value of $|\hat{k} - k|$ of the DCOM scheme is very close to that of the COM6 scheme, even for the case with $N_k = 4$ and without any correction step. The inclusion of the correction step further improves the result towards the COM6 scheme.

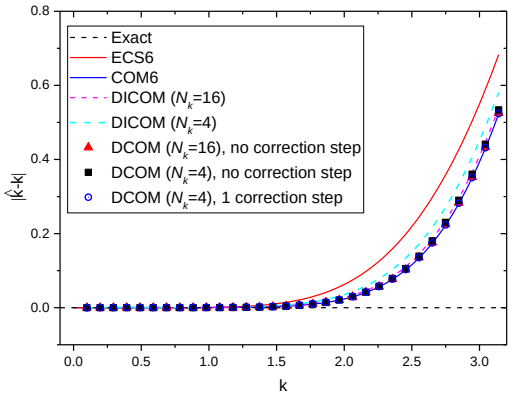

Figure 4: Meanvalues of $|\hat{k} - k|$ of sixth-order central schemes for second derivative.

It can be seen that the proposed DCOM scheme possesses superior characteristics in wavenumber space compared to the DICOM scheme. The spectral performance of the DCOM scheme is close to the fully coupled compact scheme.

4 Numerical Tests

In this section, the DCOM6 schemes are going to be tested in solving both Euler and Navier-Stokes (N-S) equations with the in-house finite difference solver: ASTR. The schemes are first tested for a 2-D vorticity wave convection/diffusion problem and then implemented for the 3-D Taylor-Green vortex problem. The correction step is not implemented for all tested cases, due to

the close accuracy of the DCOM schemes with and without the correction step and the extra computing costs of the correction step.

4.1 Governing Equations

The 3-D unsteady compressible N-S equations are used in the present paper. The equations are non-dimensionalised with the following reference quantities: length L_0, velocity u_0, temperature T_0, density ρ_0, and dynamic viscosity μ_0. The resulting dimensionless parameters are Reynolds number $Re = \rho_0 u_0 L_0/\mu_0$ and Mach number $M = u_0/\sqrt{\gamma R T_0}$. A constant Prandtl number $\mathrm{Pr} = \mu C_P/\vartheta = 0.72$ is used, where $C_P = \gamma R/(\gamma - 1)$ is the specific heat capacity of the gas at constant pressure and ϑ is the thermal conductivity. Parameters $R = 287.1\ J/(Kg \cdot K)$ and $\gamma = 1.4$ are the specific gas constant and the specific heat capacity ratio, respectively. This set of N-S equations are written in strong conservation form as,

$$\begin{gathered} \frac{\partial \rho}{\partial t} + \frac{\partial \rho u_i}{\partial x_i} = 0 \\ \frac{\partial \rho u_i}{\partial t} + \frac{\partial \left(\rho u_i u_j + p\delta_{ij}\right)}{\partial x_j} = \frac{\partial \sigma_{ij}}{\partial x_j} \\ \frac{\partial \rho e}{\partial t} + \frac{\partial (\rho e + p) u_j}{\partial x_j} = \frac{\partial \left(\sigma_{ij} u_i - q_j\right)}{\partial x_j} \end{gathered} \tag{22}$$

The standard Einstein summation notation is used and notations x_i and u_i, $i = 1,2,3$ are adopted to represent (x, y, z) and (u, v, w), respectively. The stress tensor and the heat flux vector are expressed as,

$$\sigma_{ij} = \frac{\mu}{\mathrm{Re}}\left(\frac{\partial u_i}{\partial x_j} + \frac{\partial u_j}{\partial u_i} - \frac{2}{3}\delta_{ij}\frac{\partial u_k}{\partial x_k}\right), \tag{23}$$

and

$$q_i = -\frac{\mu}{\mathrm{PrRe}(\gamma - 1)M^2}\frac{\partial T}{\partial x_i}. \tag{24}$$

The dynamic viscosity coefficient μ is calculated via Sutherland's law:

$$\mu = T^{1.5}\frac{T_S/T_0 + 1}{T + T_S/T_0}. \tag{25}$$

The convective terms are solved in the skew-symmetric form [15] and the diffusion terms are solved in the Laplacian form [16] to improve the stability of the solver. Time integration is conducted using the classic 3-step 3rd-order TVD Runge-Kutta scheme [17].

4.2 2-D Vorticity Convection and Diffusion

We first conduct a 2-D vorticity convection and diffusion problem in a uniform flow to test the developed schemes. The 2-D domain with the sizes of $L_x \times L_y = [0,20] \times [0,10]$, is discretised with a 256×128 uniform equidistant mesh and divided into 64×2 subdomains. Therefore, there are only 5 nodes ($N_k = 4$) in each subdomain in the x direction. Both Euler equations and N-S equations with periodic boundary conditions applied at all boundaries are solved with 128 MPI tasks. For the Euler equations the DCOM scheme for the first derivative is tested, while for the N-S equations the DCOM schemes for both first and second derivatives are tested.

The initial velocity and pressure are set as,

$$u = u_0 - C_{vs}\frac{y - y_c}{R_{vs}^2}e^{\frac{-r}{2}},$$
$$v = C_{vs}\frac{x - x_c}{R_{vs}^2}e^{\frac{-r}{2}}, \tag{26}$$
$$p = p_0 - 0.5\rho_0\frac{C_{vs}^2}{R_{vs}^2}e^{-r},$$

in which $x_c = 10$, $y_c = 5$ is the initial location of the vortical core; $R_{vs} = 1$, and $C_{vs} = 0.01u_0R_{vs}$ specify the strength and size of the initial vortex. The Mach number based on u_0 is 0.5 and the Reynolds number based on R_{vs} is 100 (only for solving N-S equations).

Figure 5 and Figure 6 show the flow fields at $t = 200$ (i.e. $10\,L_x/u_0$) for Euler and N-S equations, respectively. For both cases, smooth flow fields are acquired and no wiggles at the interfaces can be seen. This can be further validated by comparing vorticity profiles along central lines in the x- and y-directions in Figure 7. The profiles along the two central lines collapse well for the inviscid case. For the viscous case, the vortex becomes larger and weaker due to the effect of diffusion. The x-profile is not on top of the y-profile due to the interaction between the upper part and lower part of the vortex through the periodic condition in the y-direction. The results in Figure 7 presents wiggle-free profiles, confirming the effectiveness of the DCOM scheme for the second derivative terms. The comparison of the y-velocity and vorticity along the x central line is shown in Figure 8. The profiles of the inviscid solution overlap well with the initial profiles. The viscous solutions, however, give damped profiles as expected.

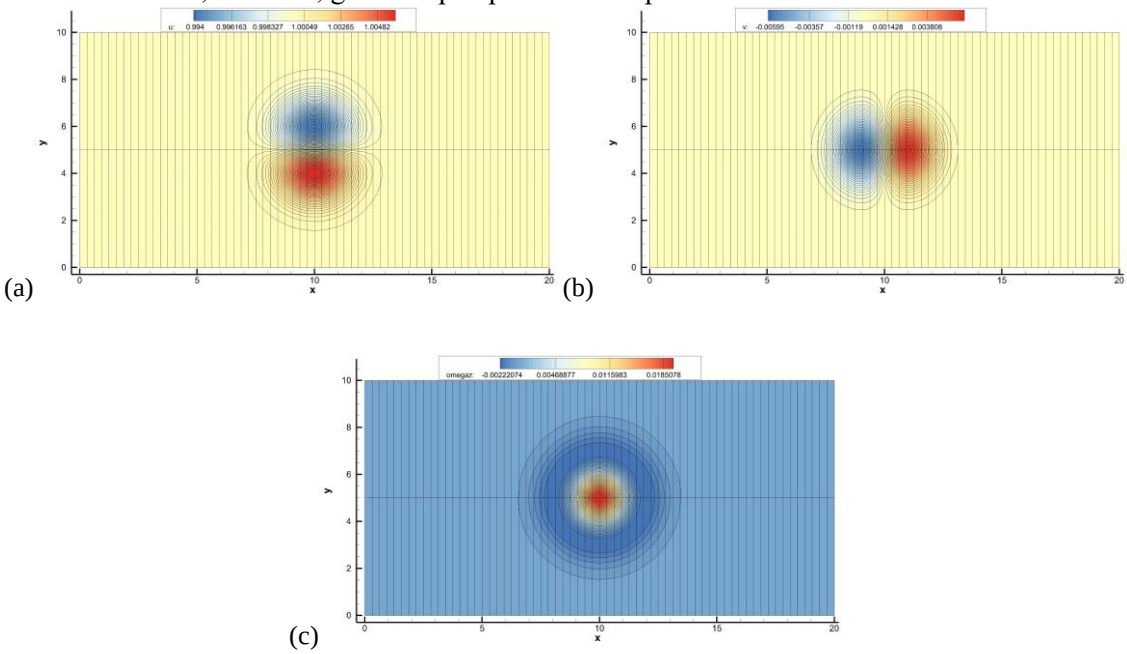

Figure 5: Inviscid flow field at $t = 200$. (a): x-velocity; (b): y-velocity; (c): vorticity. The mesh lines indicate interfaces of each subdomain.

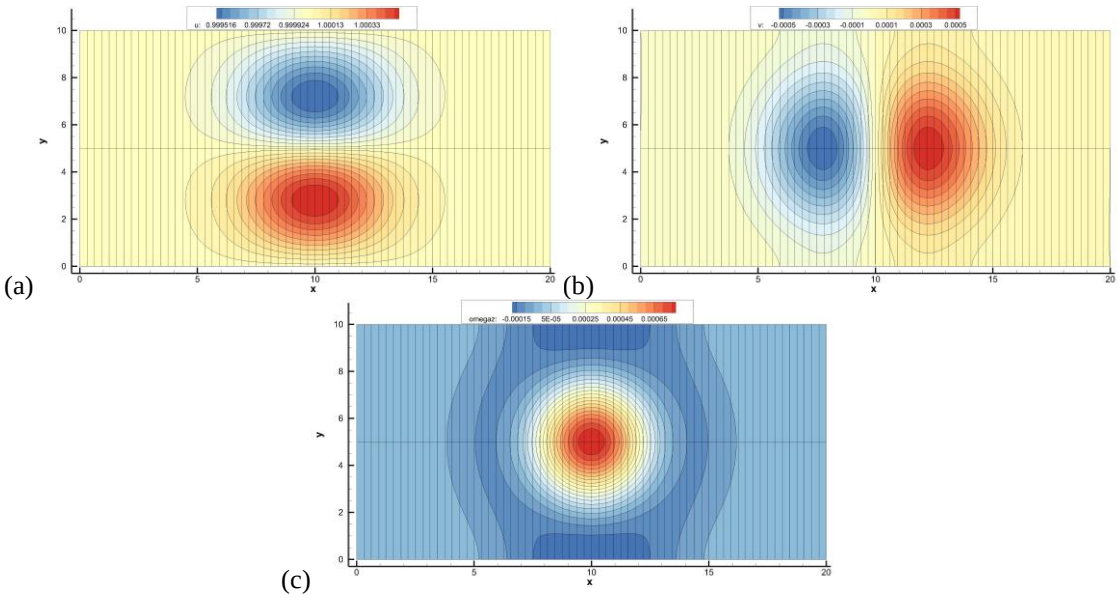

Figure 6: Viscous flow field at $t = 200$. (a): x-velocity; (b): y-velocity; (c): vorticity. The mesh lines indicate interfaces of each subdomain.

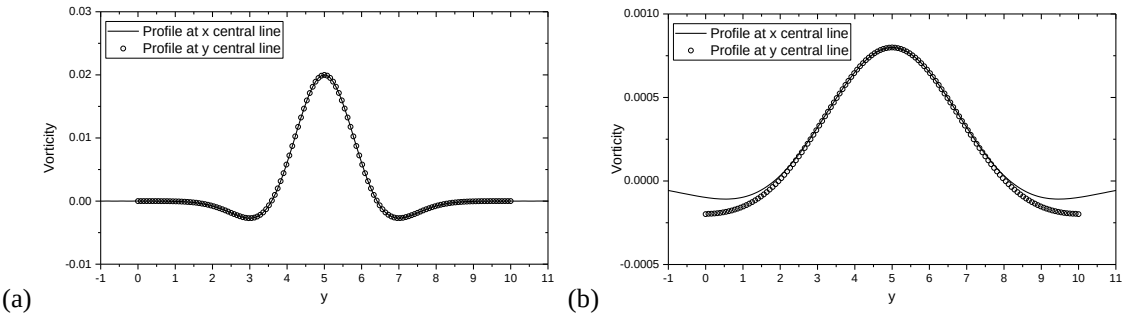

Figure 7: Profiles of vorticity at the central line. (a): inviscid solution, (b) viscous solution. Profiles at the x central line are shifted -5.

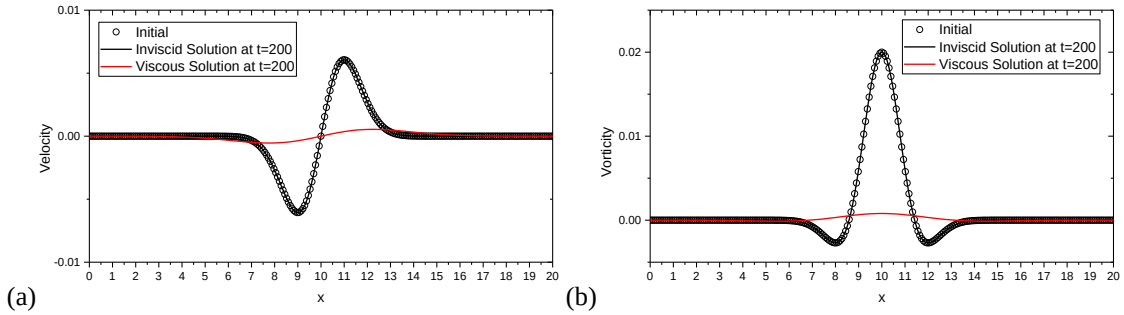

Figure 8: Profiles of vorticity (a) and y-velocity (b) at the central line ($y = 0$) at $t = 200$.

4.2 Taylor-Green Vortex Problem

The DCOM schemes are further tested for the 3-D Taylor-Green Vortex problem by solving the N-S equations in a $2\pi L$ cube domain. A 256^3 uniform mesh is used to discretise the domain and the computation is parallelised with 768 MPI tasks ($12 \times 8 \times 8$).

The initial condition is set as [18],

$$u = u_0 \sin(x/L_0)\cos(y/L_0)\cos(z/L_0),$$
$$v = -u_0 \cos(x/L_0)\sin(y/L_0)\cos(z/L_0),$$
$$w = 0, \tag{27}$$
$$p = p_0 + \frac{\rho_0 u_0^2}{16}[\cos(2\,x/L_0) + \cos(2\,y/L_0)][\cos(2\,z/L_0) + 2].$$

The Mach number based on u_0 is 0.1 and the Reynolds number based on u_0 and L_0 is 1600.

The evolution of spatially averaged kinetic energy and enstrophy acquired with the DCOM6 schemes are compared to those obtained with the pseudo-spectral method [19] on a 512^3 node mesh, shown in Figure 9. Both the kinetic energy and enstrophy profiles agree with the data from the pseudo-spectral code, and a slight underprediction of the enstrophy peak value by the DCOM6 schemes is observed. The 3-D fields of enstrophy and coherent structures visualised with iso-surfaces of swirling strength λ_{ci} (i.e. the imaginary part of the complex eigenvalue of the velocity gradient tensor) [3,20] at $t = 0$, 10, and 20 are shown in Figure 10 and Figure 11, respectively. The flow structures evolve into smaller vortical structures with higher vorticity at $t = 10$. From $t = 10$ to $t = 20$, the vortical structures become more chaotic, occupying a greater space, although the maximum strength of the enstrophy is reduced. At $t = 0$, 10 and 20, the symmetry of the flow field is well preserved.

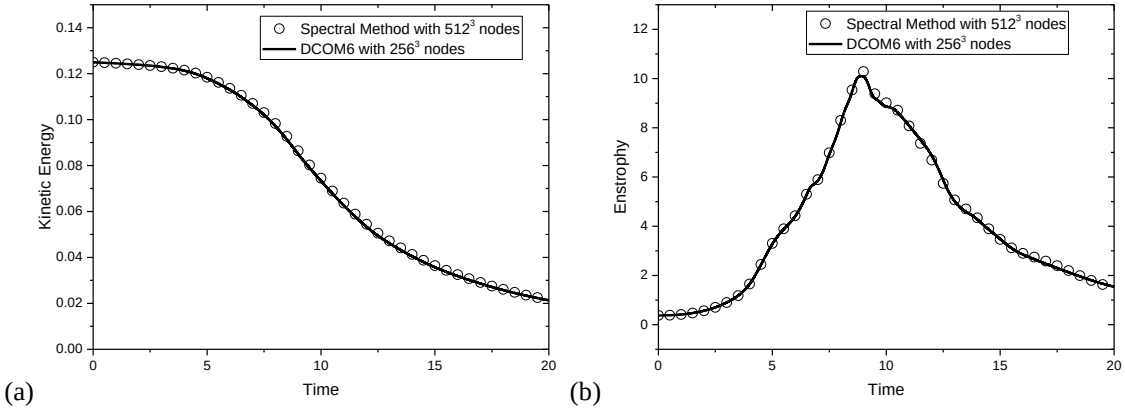

(a) (b)

Figure 9: Temporal evolution of kinetic energy (a) and enstrophy (b).

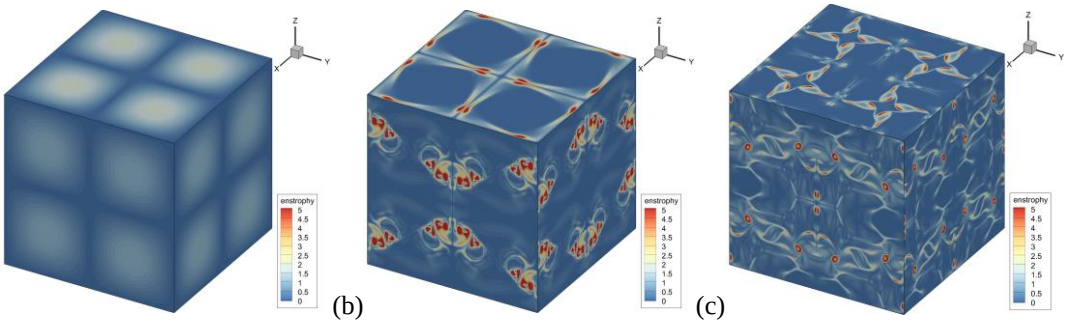

(a) (b) (c)

Figure 10: Enstrophy field at $t = 0$ (a), $t = 10$ (b) and $t = 20$ (c).

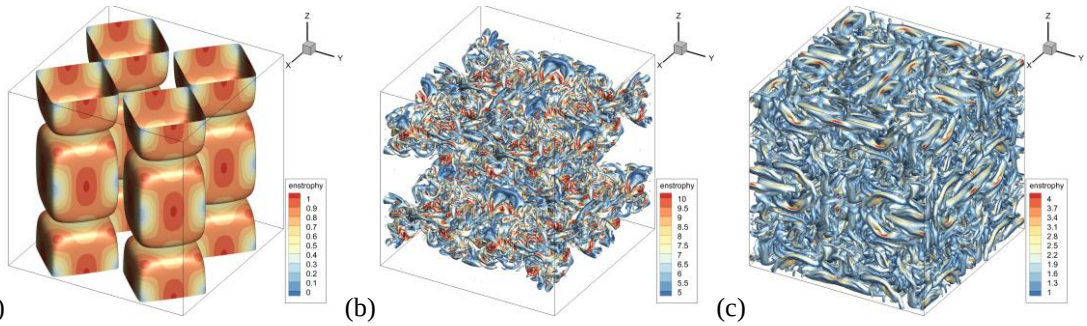

(a) (b) (c)

Figure 11: Vortical structures visualized with iso-surfaces of λ_{ci} equaling to 1% of its maximum and colored with enstrophy. (a): $t = 0$, (b): $t = 10$, (c): $t = 20$.

4.3 Scalability

The scalability of the DCOM schemes in the TGV problem is evaluated on UK National High-Performance Computing Facility ARCHER [21] with up to 12288 cores (Xeon E5-2697 v2). The wall time consumption per step (this is obtained by averaging the wall time consumed for 100 steps.) with different numbers of cores are listed in Table 1 , and the data are plotted in Figure 12. A clear linear acceleration with a 0.89 slope is obtained, indicating that the proposed schemes are well adapted to domain-decomposition-based parallel computation.

Table 1. Scalability of DCOM scheme based on ASTR code and ARCHER machine

HPC Nodes	Cores	Time per step (s)	Speedup
4	96	4.53	1
8	192	2.29	1.97
16	384	1.17	3.86
32	768	0.55	8.18
64	1536	0.32	14.32
128	3072	0.19	23.91
256	6144	0.11	41.46
512	12288	0.071	63.45

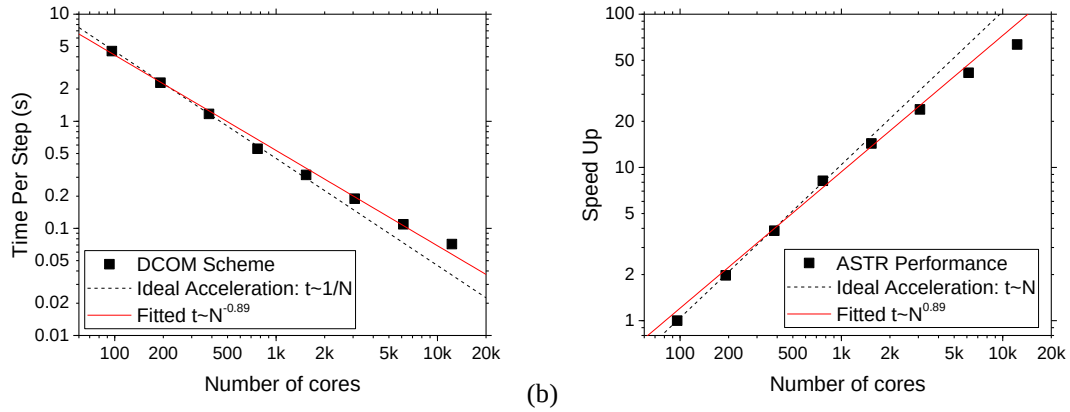

(a) (b)

Figure 12: Time per step (a) and speedup (b).

5 Summary and Conclusions

A class of domain-decoupled compact schemes for first and second derivatives is proposed for domain-decomposition-based parallel computational fluid dynamics. The compact scheme is decoupled at the interface of the subdomain and the tridiagonal matrix system is closed using the explicit scheme of the same order in halo nodes. The accuracy of the scheme can be further improved with correction steps, at increased costs of computing resources. The Fourier analysis has shown that the DCOM schemes possess close spectral properties to the fully coupled compact schemes, especially with one step of correction.

The sixth-order DCOM schemes are then assessed in the 2-D vortex convection/diffusion problem, and a 3-D Taylor-Green Vortex problem. The results have proved that the proposed scheme generates stable results for all test cases. Good agreement of the results by the DCOM6 schemes with the data obtained by the spectral method are also observed. The scalability of the proposed schemes is also evaluated based on the ASTR code and ARCHER machine with up to 12288 cores, showing that a linear speed-up can be achieved.

Acknowledgement

The project is supported by the UK Consortium on Turbulent Reacting Flows (Grant number EP/K024574/1) and the UK Turbulence Consortium (Grant number EP/L000261/1) via EPSRC. The authors also would like to thank the EPSRC for the use of ARCHER and the STFC Hartree Centre for providing computing times.

References

[1] S. K. Lele. Compact finite difference schemes with spectral-like resolution. J. Comput. Phys., 103:16-42, 1992.
[2] S. Laizet and E. Lamballais. High-order compact schemes for incompressible flows: A simple and efficient method with quasi-spectral accuracy. J. Comput. Phys., 228: 5989–6015, 2009.
[3] S. Pirozzoli, M. Bernardini and F. Grasso. Characterization of coherent vortical structures in a supersonic turbulent boundary layer. J. Fluid Mech., 613: 205–231, 2008.
[4] M. R. Visbal and D. P. Rizzetta. Large-Eddy Simulation on Curvilinear Grids Using Compact Differencing and Filtering Schemes. J. Fluid Eng., 124: 836–847, 2002.
[5] S. Nagarajan, S. K. Lele and J. H. Ferziger. A robust high-order compact method for large eddy simulation. J. Comput. Phys., 191: 392-419, 2003.
[6] R.D. Sandberg. Direct Numerical Simulations for Flow and Noise Studies. Procedia Eng., 61: 356 – 362, 2013
[7] X. Guo and L. Zhang. Symmetric super compact difference scheme of the Navier-Stokes equation and its parallel algorithm. Chin. J. Comput. Phys., 5: 281-289, 2006.
[8] X. H. Sun. Application and accuracy of the parallel diagonal dominant algorithm. Parallel Comput., 21: 1241–1267, 1995.
[9] J. Hofhaus and E. F. Van de Velde. Alternating-direction line-relaxation methods on Multicomputers. SIAM J. Sci. Comput., 17: 454–478, 1996.
[10] T.K. Sengupta, A. Dipankar and A. K. Rao. A new compact scheme for parallel computing using domain decomposition. Journal of Computational Physics, 2007, 220: 654–677.
[11] J. Chao, A. Haselbacher, and S. Balachandar, A massively parallel multi-block hybrid compact–WENO scheme for compressible flows, J. Comput. Phys., 228: 7473–7491, 2009.
[12] J. W. Kim and R. D. Sandberg. Efficient parallel computing with a compact finite difference scheme. Comput. Fluids, 58: 70–87, 2012.
[13] A. P. S. Wheeler and R. D. Sandberg. Numerical investigation of the flow over a model transonic turbine blade tip. J. Fluid Mech., 803: 119-143, 2016.
[14] R. Pichler, V. Michelassi, R. Sandberg and J. Ong. Highly resolved large eddy simulation study of gap size effect on low-pressure turbine stage. J. Turbomach., 40: 021003, 2018.
[15] C. A. Kennedy and A. Gruber. Reduced aliasing formulations of the convective terms within the Navier–Stokes equations for a compressible fluid. J. Comput. Phys., 227: 1676–1700, 2008.
[16] N. D. Sandham, Q. Li and H. C. Yee. Entropy Splitting for High-Order Numercial Simulation of Compressible Turbulence. J. Comput. Phys., 178: 307–322, 2002.
[17] S. Gottlieb and C. W. Shu. Total variation diminishing Runge-Kutta schemes. Math Comput., 67: 73–85, 1998.

[18] J. R. DeBonis. Solutions of the Taylor-Green Vortex Problem Using High-Resolution Explicit Finite Difference Methods. 51st AIAA Aerospace Sciences Meeting, AIAA paper 2013-0382, 2013.
[19] W. M. van Rees, A. Leonard, D. I. Pullin and P. Koumoutsakos. A comparison of vortex and pseudo-spectral methods for the simulation of periodic vortical flows at high Reynolds numbers. J. Comput. Phys., 230: 2794-2805, 2011.
[20] J. Zhou, R. J. Adrian, S. Balachandar and T. M. Kendall. Mechanisms for generating coherent packets of hairpin vortices in channel flow. J. Fluid Mech., 387: 353-396, 1999.
[21] http://www.archer.ac.uk/about-archer/hardware/